chemosensors

MDPI

Article

Experimental-Theoretical Approach for the Chemical Detection of Glyphosate and Its Potential Interferents Using a Copper Complex Fluorescent Probe

Guilherme Martins [1], Karolyne V. Oliveira [1], Saddam Weheabby [2], Ammar Al-Hamry [2], Olfa Kanoun [2], Tobias Rüffer [3], Benedito J. C. Cabral [1,4] and Leonardo G. Paterno [1,*]

[1] Laboratory of Research on Polymers and Nanomaterials, Institute of Chemistry, University of Brasilia, Brasília 70910-900, DF, Brazil; bjcabral@fc.ul.pt (B.J.C.C.)
[2] Professorship Measurement and Sensor Technology, Chemnitz University of Technology, 09126 Chemnitz, Germany
[3] Faculty of Natural Sciences, Institute of Chemistry, Inorganic Chemistry, Chemnitz University of Technology, 09107 Chemnitz, Germany
[4] BioISI-Biosystems and Integrative Sciences Institute, Departamento de Química e Bioquímica, Faculdade de Ciências, Universidade de Lisboa, 1749-016 Lisboa, Portugal
* Correspondence: lpaterno@unb.br

Abstract: The present contribution proposes an optical method for the detection of glyphosate (GLY) using a Cu(II) bis-(oxamate) complex ($[Cu(opba)]^{2-}$) as the fluorescent probe. It wa found that in acetonitrile solution, its fluorescence increases in the presence of GLY and scales linearly (R^2 = 0.99) with GLY concentration in the range of 0.7 to 5.5 μM, which is far below that established by different international regulations. The probe is also selective to GLY in the presence of potential interferents, namely aminomethyl phosphonic acid and *N*-nitrosoglyphosate. Theoretical results obtained by time-dependent density functional theory coupled to a simplified treatment of the liquid environment by using a self-consistent reaction-field revealed that GLY molecules do not coordinate with the central Cu^{2+} ion of $[Cu(opba)]^{2-}$; instead, they interact with its peripheral ligand through hydrogen bond formation. Thereby, GLY plays mainly the role of the proton donor. The results also suggest that GLY increases the dielectric constant of the medium when it contributes to the stabilization of the excited state of the $[Cu(opba)]^{2-}$ and enhancement of its fluorescence.

Keywords: copper complexes; dielectric medium; fluorescent sensor; herbicides; hydrogen bonding

Citation: Martins, G.; Oliveira, K.V.; Weheabby, S.; Al-Hamry, A.; Kanoun, O.; Rüffer, T.; Cabral, B.J.C.; Paterno, L.G. Experimental-Theoretical Approach for the Chemical Detection of Glyphosate and Its Potential Interferents Using a Copper Complex Fluorescent Probe. *Chemosensors* **2023**, *11*, 194. https://doi.org/10.3390/chemosensors11030194

Academic Editor: Guo-Hui Pan

Received: 9 February 2023
Revised: 4 March 2023
Accepted: 14 March 2023
Published: 16 March 2023

1. Introduction

Glyphosate (GLY) (IUPAC name: *N*-(phosphonomethyl) glycine), Scheme 1, is a systemic herbicide used to eliminate several types of weeds and grasses that compete with crops. It inhibits the synthesis of 5-enolpyruvyl-shikimate-3-phosphate synthase, which is an essential enzyme for the biosynthesis of aromatic amino acids in plants [1,2]. Since its discovery by Monsanto in 1970, GLY and GLY-based products have been widely used globally [3]. Previously thought to be harmless, recent studies have reported their toxicity to several aquatic species and humans, with effects including carcinogenic and endocrine disruption [4]. This is concerning, as GLY residues have been found in crops, food, and the environment, including soil, groundwater, surface waters, marine sediments, seawater, rain, and air [5].

Despite this, detecting GLY is a challenging task because the GLY molecule is insoluble in common organic solvents, has low electroactivity, and lacks chromophore/fluorophore groups. Conventional instrumental analysis can only be performed on its derivatized products, making the process time-consuming and expensive. For example, derivatized GLY has been detected by GC-UV or HPLC-UV [6], fluorescence [7], mass quadrupole (HPLC-ICP-MS/MS) [8], and ^{1}H NMR [9]. Alternative approaches, such as ELISA [10,11],

SERS [12], and electrochemical sensors [13] have been employed without requiring previous derivatization procedures. However, these methods are generally slow, fail to detect GLY and its metabolites simultaneously, or can be influenced by cross-reactions with common interfering species. Therefore, there is a high demand for the development of fast and reliable methods for GLY detection.

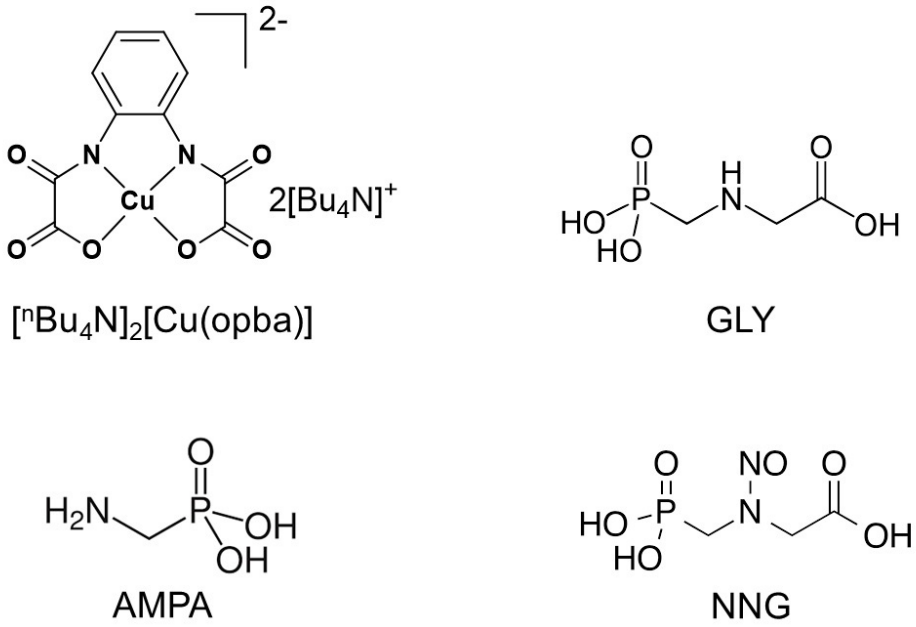

Scheme 1. Structural formulae of $[^{n}Bu_4N]_2[Cu(opba)]$, GLY, AMPA, and NNG.

Optical detection of GLY has been proposed as an alternative methodology and has provided promising results [14]. In this method, absorption and/or luminescence of a molecular probe are turned on/off upon interaction with the analyte, thus permitting a more straightforward visual analysis. Besides that, its practical implementation can be accomplished with miniaturized photometric devices and readout systems using user-friendly interfaces, such as smartphones [15]. This strategy may allow for on-site and real-time monitoring, thereby enabling environmental control and surveillance more expeditiously. Since many of these electronic and computing platforms are well-developed and readily available, the main challenge of this research field still relies on the development of sensitive and selective probes. The literature collects several examples of such systems for detecting GLY and similar compounds, including carbonaceous and metallic nanoparticles [16–18] as well hybrid systems comprising biological recognition elements conjugated to an optical probe [19,20]. The level of sophistication follows the need for sensitive and more selective devices, since the detection of not only GLY but also its metabolites is equally important.

Among different detection strategies, the interaction between a probe, Cu^{2+} ions and GLY has been recently investigated [21–23]. It is known that GLY molecules strongly coordinate to metal ions [24] and, indeed, this is a matter of environmental concern, as such an interaction makes GLY capable of adsorbing onto clay minerals [25,26]. Additionally, it hampers its natural degradation and prevents its detection without applying pretreatment methods. On the other hand, some elegant approaches for GLY detection, harnessing this complexing capacity, have been proposed. Gui et al. [21] synthesized two polyacetylene probes containing triazole and benzoimidazole side groups, whose fluorescent emission in solution is quenched upon interaction with Cu^{2+} ions by means of either electron or energy transfer processes. When GLY is added to the solution, it rapidly coordinates with Cu^{2+} and the probe emission is restored. This restoration scales with the GLY concentration, and the derived method shows a limit of detection (LOD) of 80 nM. In a similar approach, Sun et al. [22] designed a naphthalimide complex whose fluorescence is quantitatively

quenched by Cu^{2+} and rapidly restored in the presence of GLY. The method detected GLY in the linear range of 10–100 μM with an LOD of 1.87 μM. Wang et al. [23] developed a coumarin Cu^{2+} probe capable of detecting GLY by a similar turn off-on-off mechanism within a linear range of 118–887 nM and LOD of 108 nM.

Herein, we propose a different way for the fluorescent detection of GLY. The sensor probe is a Cu(II) bis(oxamate) complex, $[^nBu_4N]_2$[Cu(opba)], where BuN_4 = tetrabutylammonium and opba = *o*-phenylenebis(oxamate), abbreviated as $[Cu(opba)]^{2-}$ (Scheme 1), whose fluorescence is enhanced in the presence of GLY and marginally affected by potential interfering agents including aminomethyl phosphonic acid (AMPA) and *N*-nitrosoglyphosate (NNG), also shown in Scheme 1. Time-dependent density functional theory (TDDFT) calculations were also carried out for the absorption and emission spectra of individual $[Cu(opba)]^{2-}$ and GLY in liquid acetonitrile and also in $[Cu(opba)]^{2-}$-GLY complex. The solvent molecules were represented using an implicit solvent model based on a self-consistent reaction field (SCRF) and micro-solvation approaches. The micro-solvation approach, at least for small $[Cu(opba)]^{2-}$-GLY aggregates, indicates that GLY molecules do not coordinate with the central Cu^{2+} ion of $[Cu(opba)]^{2-}$; instead, they interact with its peripheral ligand through hydrogen bonding, where GLY plays mainly the role of proton donor. The importance of hydrogen bonding in the control of photophysical properties for anionic species was recently discussed [27]. Moreover, simulations also suggest that GLY increases the dielectric constant of the medium, thereby contributing to the stabilization of the excited state of $[Cu(opba)]^{2-}$ and thus increasing its fluorescence.

2. Materials and Methods

2.1. Materials

All chemicals used for the synthesis of $[^nBu_4N]_2$[Cu(opba)]$^{2-}$ and preparation of solutions were of analytical grade and used as received. Certified standards of GLY, AMPA and NNG as well as spectroscopic grade acetonitrile (ACN) were purchased from Sigma-Aldrich (St. Louis, MO, USA) and used without any further purification. All water employed in sample preparations was ultrapure (resistivity: 18 MΩ cm).

2.2. Synthesis of the $[^nBu_4N]_2$[Cu(opba)]

The complex was synthesized following the procedure published in Ref. [28] with slight modifications. In brief, 5 g (1 mmol) of *o*-phenylenebis(oxamic acid) diethyl ester was suspended in 150 mL of a 4:1 water:ethanol mixture and mixed with $[^nBu_4N]OH$ (4 mmol). The reaction mixture was stirred and heated to 60 °C for 15 min. After cooling to room temperature, a solution of $CuCl_2 \cdot 2H_2O$ (2.79 g, 1 mmol) in 30 mL of H_2O was added dropwise with continuous stirring. The reaction mixture was stirred for an additional 30 min. The resulting mixture was then extracted with CH_2Cl_2 (3 × 100 mL), and the combined organic phase was washed with H_2O (3 × 100 mL). After drying over anhydrous Na_2SO_4, the solvent was evaporated to dryness to yield the desired deep-purple complex.

2.3. Structural Characterizations and Herbicide Fluorescence Detection

The molecular structure of $[^nBu_4N]_2$[Cu(opba)] was determined using a variety of spectroscopic techniques. FTIR spectra were recorded on a Perkin-Elmer Spectrum 1000 FT-IR in the range of 400–4000 cm^{-1} using KBr pressed pellets. Raman spectra were obtained using an InVia Raman Renishaw instrument with a 632.8 nm laser, 25 mW. The acquisition was performed with a CCD detector and Leica microscope (50× objective lens) in backscattering configuration, 1200-lines/mm grating, and resolution of 1 cm^{-1}. UV-Vis absorption spectra were recorded on a Varian Cary 5000 spectrophotometer, whereas fluorescence emission spectra were registered in static mode with a Horiba Scientific Fluorlog-3 spectrofluorometer.

Absorption spectra of plain diluted solutions (0.2 mM) of $[^nBu_4N]_2$[Cu(opba)] were registered in ACN, whereas spectra of plain GLY, AMPA and NNG were registered in ultrapure water. The following measurement conditions were adopted: optical path:

10 mm (quartz cuvette); range: 200–800 nm; scan rate: 600 nm/min; resolution: 1 nm. In a second experiment, the spectra of $[^nBu_4N]_2$[Cu(opba)] mixed with GLY at molar ratios of 1:1, 1:2 and 1:4 were recorded under the same conditions to match the configurations using theoretical calculations.

Emission spectra were registered in steady-state mode using quartz cuvette of 10 mm optical path with four polished windows. Initially, emission spectra of the $[^nBu_4N]_2$[Cu(opba)] solution in ACN (0.2 mM) were registered under different excitation wavelengths (290–350 nm) with optimized measuring conditions (integration time: 0.2 s; slits: 5 nm; grating: 1200 gr/mm; resolution: 2 nm). For GLY detection, 10 µL aliquots of an aqueous GLY stock solution (177 µM) were successively added to the $[^nBu_4N]_2$[Cu(opba)] solution (2 mL, 0.2 mM). The GLY concentrations ranged from 0.7 µM to 5.5 µM. The solution of $[^nBu_4N]_2$[Cu(opba)] and GLY was manually stirred after every addition of GLY, and the spectra were registered under the following optimized conditions: excitation: 340 nm; integration time: 0.2 s; slits: 5 nm; grating: 1200 gr/mm; resolution: 0.5 nm. In a second experiment, the spectra of $[^nBu_4N]_2$[Cu(opba)] mixed with GLY at three different molar ratios (1:1, 1:2 and 1:4) were measured under the same conditions to match the configurations evaluated in the theoretical calculations. To study the interference, different aliquots of interfering agents, namely AMPA and NNG, were added to a stock solution containing $[^nBu_4N]_2$[Cu(opba)] (0.2 mM) and GLY (2.8 µM). The concentrations of each interfering agent were: 0.28 µM, 2.8 µM and 42 µM. The measurements were carried out under similar conditions as before.

3. Results and Discussion

3.1. Fluorescent Detection of GLY and Interference of AMPA and NNG

The synthesis of $[^nBu_4N]_2$[Cu(opba)] was the subject of previous contributions [28,29] as well its spectroscopic features [30,31]. Herein, a set of spectroscopic methods with the addition of Raman and fluorescence spectroscopy were employed. They are summarized in Figure S1 along with infrared and Raman attributions in Table S1, where its molecular structure is confirmed as proposed in Scheme 1.

Figure S2 provides the fluorescence spectra of $[Cu(opba)]^{2-}$ solution (0.2 mM) in ACN registered under different excitation wavelengths. For excitations between 240 nm and 320 nm, we observed a single sharp fluorescence signal at 370 nm that gradually decreased as the excitation wavelength increased. When the excitation exceeded that (330 and 340 nm), a second signal, broader and less intense, also appeared, at ~400 nm. The first one was ascribed to the ligand, whereas the second was assigned to a ligand to metal ($^2P_0 \leftarrow {}^2P_1$) transition. Nonetheless, as will be seen further, this latter transition was somehow assisted by the solvent due to polarization effects that stabilized its excited states.

The fluorescence spectra of the $[Cu(opba)]^{2-}$ solution (0.2 mM) in ACN mixed with increasing aliquots of GLY (10 µL of GLY stock solution at 177 µM) are shown in Figure 1a, whereas the respective analytical curve is shown in Figure 1b. It was observed that the emission at 400 nm gradually increased with the amount of added GLY in a linear fashion. It is worth mentioning that the LOD was found to be lower at that wavelength compared to other wavelengths that were tested. The linear range was set between 0.7 µM and 5.5 µM, with a corresponding analytical curve, I versus [GLY], fitted by the following equation: $I = 59{,}151 + 1.01 \times 10^{10}[GLY]$, $R^2 = 0.990$. The *LOD* was estimated as follows. First, we calculated the residual sum of squares (RSS) for the linear fit using Equation (1):

$$RSS = \sum_{i=1}^{n} (y_i - \hat{y}_i)^2 \quad (1)$$

in which y_i is the ith value of the variable to be predicted, whereas $\hat{y}_i$ is the predicted value of y_i. The *LOD* was defined by Equation (2):

$$LOD = \frac{3 \times S_{x/y}}{b} \quad (2)$$

where b is the slope of the linear fit, and $s_{x/y} = \sqrt{\frac{RSS}{N-2}}$, in which N is the number of data points. Therefore,

$$LOD = \frac{3 \times \sqrt{\frac{RSS}{N-2}}}{b} \quad (3)$$

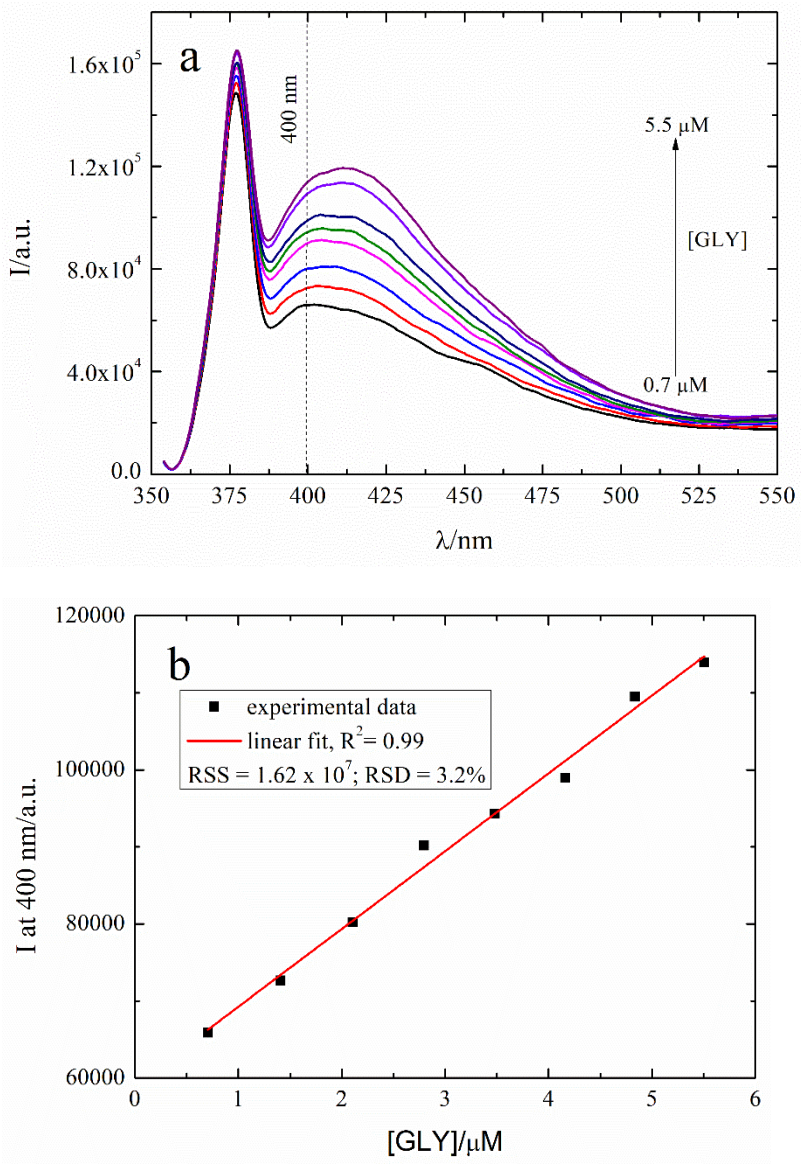

Figure 1. (**a**) Emission spectra (λ_{exc} = 340 nm) of $[Cu(opba)]^{2-}$ (0.2 mM) after successive additions of 10 µL aliquots of aqueous GLY (177 µM). (**b**) Analytical curve for the emission (I) of $[Cu(opba)]^{2-}$ as a function of GLY concentration.

According to Equation (3), LOD = 489 nM (equivalent to 82.7 ng mL^{-1}). The maximum residual limit (MRL) stablished for GLY in drinking water varies from country to country. For instance, the United States Environmental Protection Agency (EPA) sets the MRL at 700 ng mL^{-1}, while in Brazil this value is 500 ng mL^{-1}, and in Canada is 280 ng mL^{-1}. In the EU, this limit is even lower, at 100 ng mL^{-1} [5]. Therefore, the LOD achieved with the $[Cu(opba)]^{2-}$ probe meets the limits established by a considerable number of regulatory agencies. Additionally, Table 1 summarizes the sensing performance of some fluorescence-based methods for the detection of GLY, revealing that $[Cu(opba)]^{2-}$ performs reasonably well. As an advantage, $[Cu(opba)]^{2-}$ responds to GLY without needing the presence of a second chemical species, as in the case of turn-on-off-on probes listed in Table 1.

Table 1. Sensing performance of some fluorescence-based methods for the detection of GLY.

Probe	Linear Range (μM)	LOD (nM)	Reference
C-dot/Anti-GLY	0.06–473	47	[16]
C-dots	0.02–2.0	600	[17]
GQD-AgNP	0.177–11.829	53.23	[18]
DNA-CuNP	1–18	470	[19]
C-dots/AgNP	0.148–14.8	71	[20]
PAc/Cu^{2+}	-	80	[21]
NPA/Cu^{2+}	10–100	1870	[22]
CND/Cu^{2+}	0.12–8.87	10.8	[23]
$[Cu(opba)]^{2-}$	0.7–5.5	489	This work

C-dot/Anti-GLY: carbon dots labeled with a glyphosate antibody; C-dots: carbon dots; GQD-AgNP: graphene quantum dots/silver nanoparticles; C-dots/AgNP: carbon dots/silver nanoparticles; DNA-CuNP: DNA templated copper nanoparticles; PAc/Cu^{2+}: disubstituted polyacetylene/copper ion complex; NPA/Cu^{2+}: N-n-butyl-4-(3-pyridin) ylmethylidenehydrazine-1,8-naphthalimide/copper ion complex; CND/Cu^{2+}: coumarin derivative/Cu^{2+}; $[Cu(opba)]^{2-}$ ion complex

According to Lupi et al. [32], in surface soil from Buenos Aires, Argentina, one of the most important soybean production areas, AMPA, which is a GLY metabolite, can be found in the range of 0.299–2.256 μg g^{-1}, whereas GLY is found in the range of 0.035–1.502 μg g^{-1}. On the other hand, NNG has been detected as an impurity of technical glyphosate. For instance, technical glyphosate from Monsanto may contain about 0.2 mg kg^{-1} of NNG [33]. Once AMPA and NNG are found alongside GLY in different types of samples, they are, therefore, potential interferents. In order to evaluate their interfering effect, the fluorescence of $[Cu(opba)]^{2-}$ (0.2 mM) containing GLY at 2.8 μM, which is the middle point in the calibration curve shown in Figure 1b, was measured in the presence of AMPA and NNG separately, at three different concentrations: 0.28 μM, 2.8 μM and 42 μM. As shown in Figure 2, the presence of both interfering agents affected the sensing response only at the highest tested concentration, which increased the fluorescence of $[Cu(opba)]^{2-}$ further, by about 16.72% for AMPA and 12.21% for NNG. The effect of both together did not show significant differences when compared to them isolated.

3.2. Theoretical Calculations

3.2.1. Computational Details

Geometry optimizations for the isolated $[Cu(opba)]^{2-}$ dianionic complex and GLY were carried out with DFT B3LYP [34,35], with the SDD basis-set [36]. With SDD, the core electrons of Cu are represented by a Stuttgart/Dresden pseudo potential, while the electrons are described by a D95double-ζ quality basis-set [36]. The optimized $[Cu(opba)]^{2-}$ and GLY structures are illustrated in Figure 3. Vibrational frequencies were calculated for each optimized geometry and were characterized as local minima on the potential energy surface, meaning that all the frequencies were real.

The solvation of $[Cu(opba)]^{2-}$ in acetonitrile (ACN) was discussed by using an implicit solvent model based on the self-consistent reaction field method (SCRF) [37]. In this simplified but widely employed approach, the solvent is represented by a dielectric constant ε. We used a variation of polarizable continuum model (PCM) [38] called SMD [39], a self-consistent solvation model (SM) where D denotes the electronic density. The SMD is considered universal and has been parameterized for the solvation of neutral and ionic species in several solvents [39]. Specific solute–solvent interactions, such as hydrogen bonding, are not explicitly represented by SCRF methods. Therefore, to understand complex–solvent interactions, we employed a micro-solvation (MS) approach to optimize the structures of $[Cu(opba)]^{2-}$-ACN and ACN-GLY anionic clusters with a few solvent molecules. We also used a combination of the MS model with the SCRF approach, where

the optimized micro-cluster is embedded in a dielectric medium. This approach is called MS+SCRF.

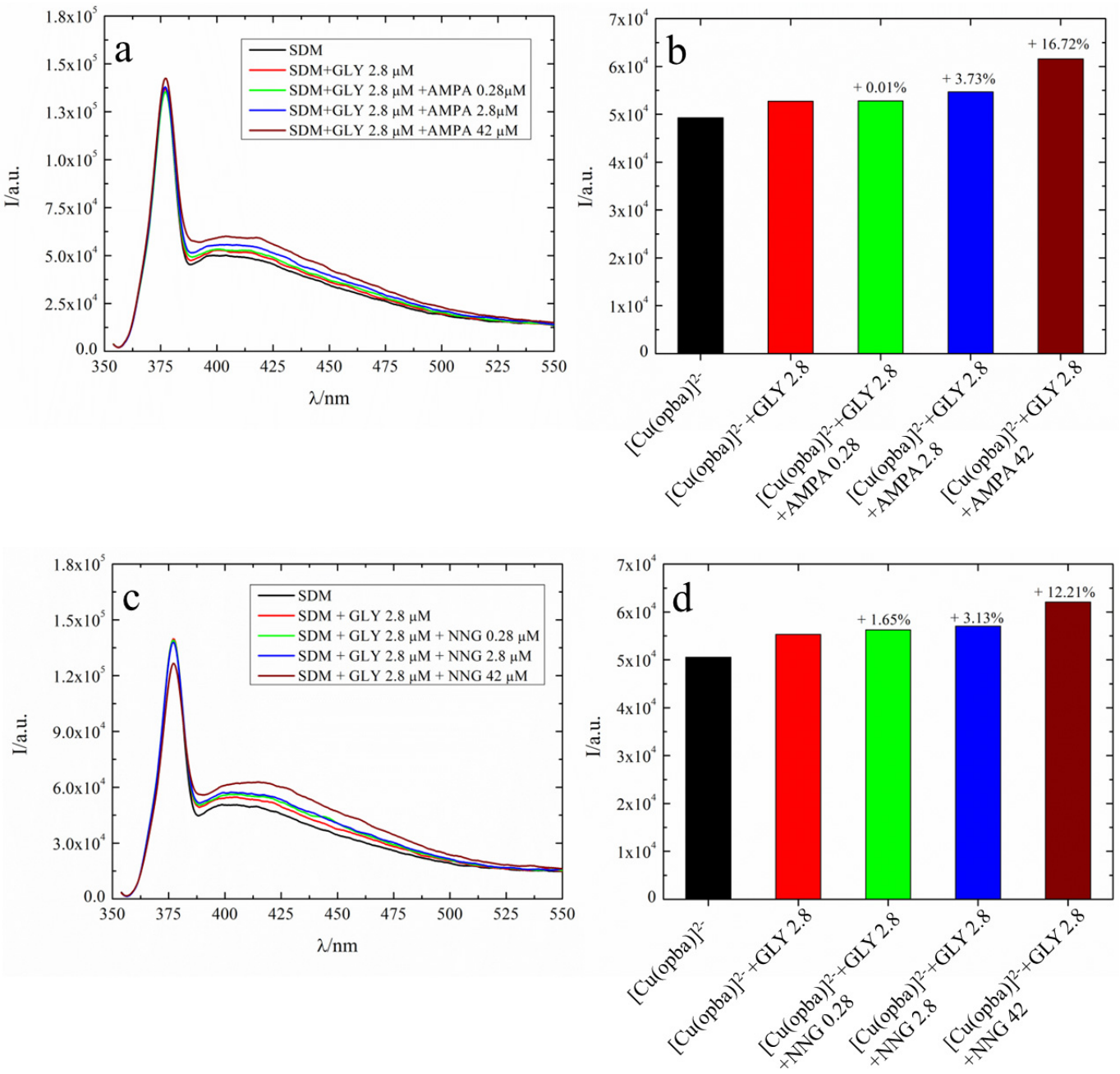

Figure 2. Emission spectra (λ_{exc} = 340 nm) of $[Cu(opba)]^{2-}$ (0.2 mM) plus GLY (2.8 μM) and interfering effect of different concentrations (0.28 μM, 2.8 μM, and 42 μM) of (**a**,**b**) AMPA and (**c**,**d**) NNG. RSD in all mixtures is below 1%.

Due to the high computational cost involved in the geometry optimization of these structures, we adopted the semi-empirical parametrized method 6 (PM6) [40]. It should be noted that solvation processes rely on the statistical mechanics sampling of different configurations at a given thermodynamic condition. However, in the present case, involving a double charged ionic species $[Cu(opba)]^{2-}$ and strong anion–solvent interaction, it was expected that optimized structures provide an acceptable representation for solvation.

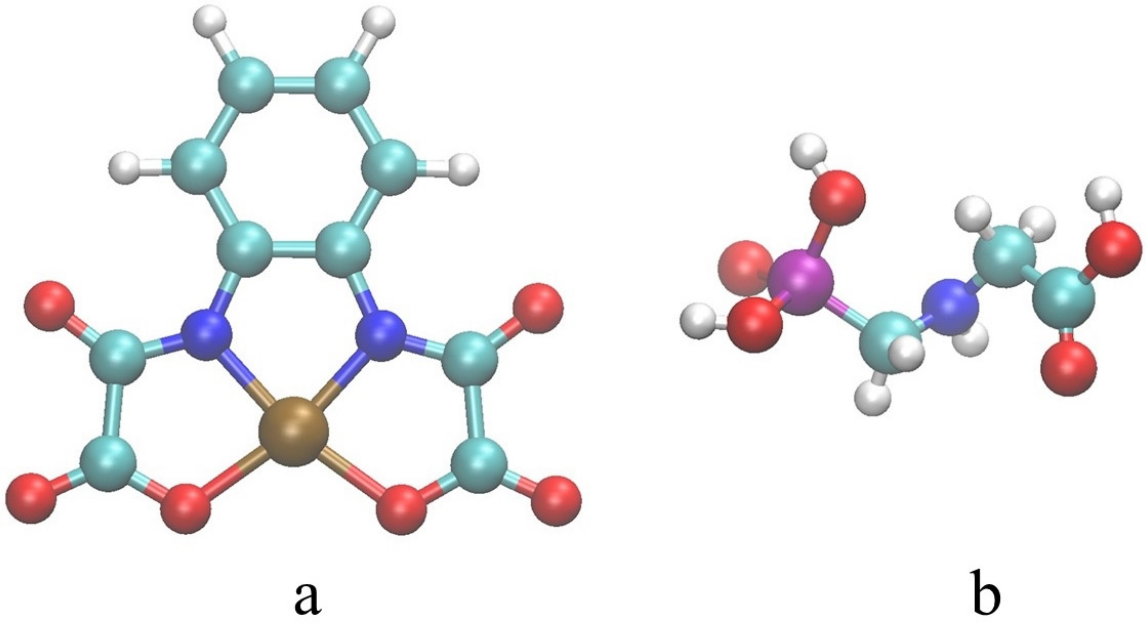

Figure 3. B3LYP/SDD optimized structures of (**a**) $[Cu(opba)]^{2-}$ and (**b**) glyphosate. Atom colors: copper (brown); carbon (cyan); nitrogen (blue); oxygen (red); hydrogen (white); phosphorous (magenta). Some bond lengths (in Å): Cu-O (1.97); Cu-N (1.94); C=O (1.27); P-O(H)=1.71; P=O (1.58).

Absorption and emission spectra were calculated with time-dependent density functional theory (TDDFT) [41]. The emission spectra calculation in ACN was carried out by performing SCRF calculations. For $[Cu(opba)]^{2-}$ in ACN, two stronger absorption bands at λ = 344.0 nm and λ = 266.5 nm were selected, and excited state geometry optimizations at the B3LYP/SDD level were carried out. Recently, the accuracy of excited state geometries predicted by DFT was investigated by Wang and Durbeej [42] for a family of dyes. It was shown that although hybrid DFT methods predict ground state geometries in good agreement with experiment and high-level ab initio methods, less accurate results are predicted for excited state geometries [42]. However, the difference between B3LYP and several other DFT hybrid methods for both ground and excited state geometries is small, thus supporting the present choice of B3LYP. We are not aware of experimental values for the dielectric constant of GLY. However, data for water–glyphosate mixtures were reported [43], and it was shown that the complex dielectric constant ε of the water–glyphosate mixtures increases with the glyphosate concentration [43]. Taking the ε of liquid water as reference, values for ε in the mixture ranged from 68.0 to 500 depending on the glyphosate concentration [43]. Similarly, a recent study published by our group [44] demonstrated that the capacitance of electronic tongue sensors, which is indicative of the dielectric constant of the medium, increases linearly with the concentration of glyphosate, similarly to the results found in this study. To model the water–glyphosate mixture, a dielectric constant of 108.9 was considered, which takes into account the increase in the dielectric constant of the mixture compared to liquid water. This value is similar to that of liquid formamide, which is parametrized in the SMD model. The strong absorption band of $[Cu(opba)]^{2-}$ in formamide at λ = 361 nm was then selected to carry out excited state geometry optimization and emission spectrum calculations.

Using SCRF, the number of excited states Ns in TDDFT for the absorption spectra was chosen as Ns = 70. However, the calculation of emission spectra based on the geometry optimization of excited states becomes difficult and computationally demanding for large molecular systems. As a result, only the absorption spectrum was calculated with the MS and MS+SCRF approaches, and in these cases, Ns = 130. All of the calculations were carried out with the Gaussian-16 suite of programs [45].

3.2.2. Absorption Spectra

Self-Consistent Reaction Field (SCRF-SMD)

Before presenting results for $[Cu(opba)]^{2-}$ in ACN and GLY, it is important to discuss how the absorption spectrum of the anionic species depends on the polarity of the solvent. The absorption spectra in different polar solvents are shown in Figure 4.

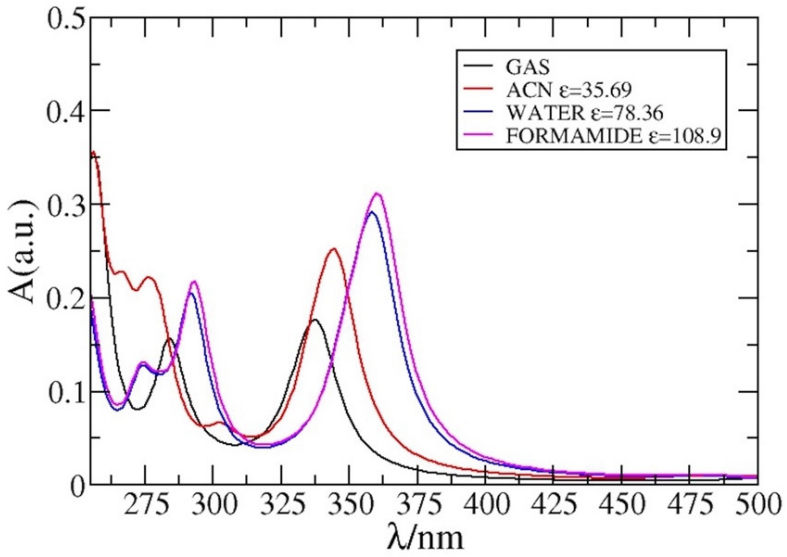

Figure 4. Absorption spectra of $[Cu(opba)]^{2-}$ for the isolated species (gas) and in polar solvents (acetonitrile, water, and formamide).

The main absorption maxima undergo a red shift with an increase in solvent polarity, as demonstrated by the absorption spectra presented in Figure 4. This red-shift is largely attributed to polarization effects that are captured by the SCRF model. The major absorption maxima for ACN and GLY (modeled using formamide) were at 344 nm and 361 nm, respectively, indicating a red shift of ~0.3 eV. The main absorption peak for the doublet-doublet transition is primarily determined by the SOMO to LUMO transition, as illustrated in Figure 5. Excitation results in a charge transfer from the Cu atom to the anionic framework.

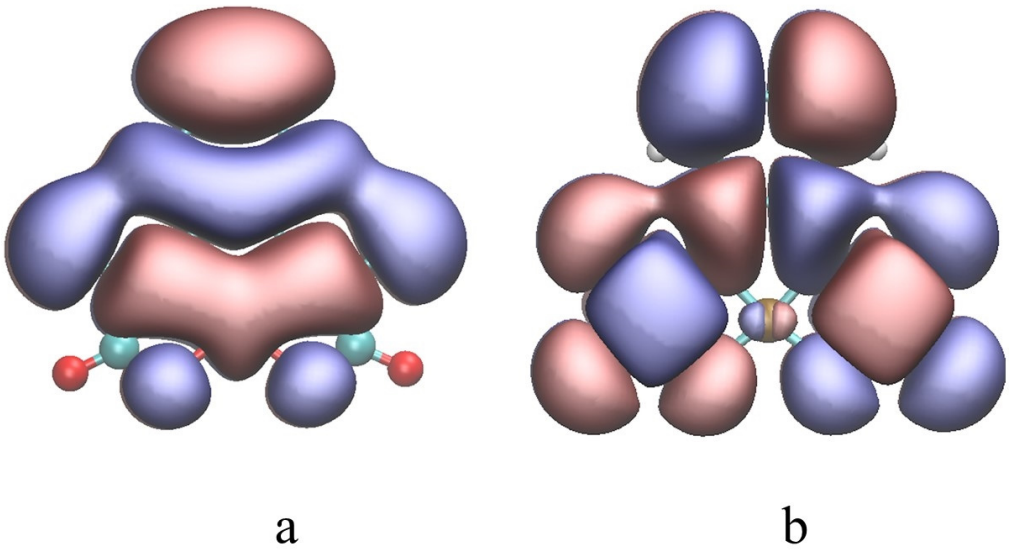

Figure 5. The (**a**) SOMO and (**b**) LUMO orbitals of $[Cu(opba)]^{2-}$ in ACN. The isodensity cutoff is 0.004 $e/a_0{}^3$.

Micro-Solvation Approach

Figure 6a illustrates the structure of the $[Cu(opba)]^{2-}$-$(ACN)_6$ complex, which shows hydrogen bonding between the anionic complex and ACN molecules. We compared the geometries obtained using PM6 and DFT B3LYP/SDD for $[Cu(opba)]^{2-}(ACN)_6$. The hydrogen bond (HB) distances differed by approximately 0.19 angstroms, while the C-O bond lengths differed by less than 0.032 angstroms. Although some differences were observed, it appears that PM6 geometries provide a good description of the $[Cu(opba)]^{2-}(ACN)_6$ complex. Figure 6b displays the absorption spectra obtained from the MS and MS+SCRF models. In comparison to MS, the MS+SCRF spectrum was red-shifted by ~6 nm. This result is consistent with the impact of long-range polarization effects, which lead to a red-shift when the dielectric constant increases (see Figure 4).

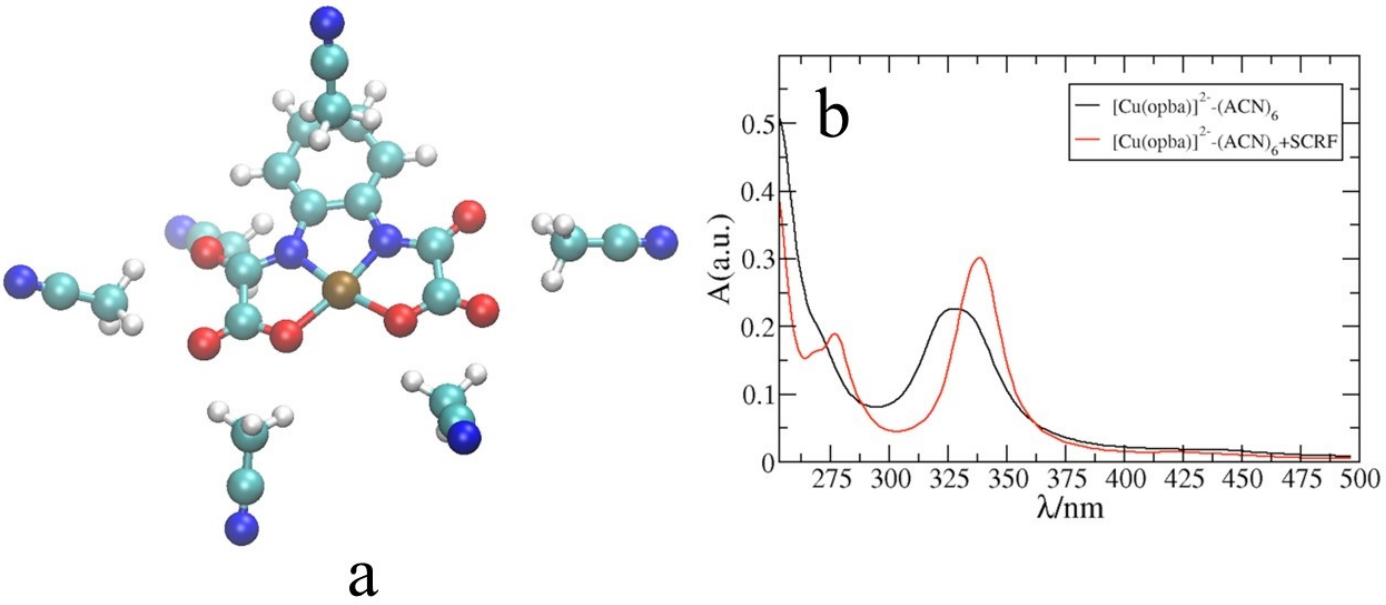

Figure 6. (**a**) $[Cu(opba)]^{2-}(ACN)_6$ B3LYP/SDD optimized structure. Atom colors: copper (brown); carbon (cyan); nitrogen (blue); oxygen (red); hydrogen (white). O ... H(ACN) hydrogen bond distances (in Å) are in the 2.03–2.05 range. (**b**) Absorption spectra from the micro-cluster (black) and micro-cluster + SCRF (red) approaches.

The optimized structures of $[Cu(opba)]^{2-}(ACN)_6$ and $(GLY)_N$ micro-clusters for N = 1, 2 are reported in Figure 7a,b. Micro-solvation of $[Cu(opba)]^{2-}$ in GLY revealed that the complexes are stabilized by hydrogen bonding. However, for the small clusters studied here, no interactions were observed between GLY and the $[Cu(opba)]^{2-}$ metallic center (the Cu(II) ion). Figure 7c reports the corresponding absorption spectra, which show a strong dependence on the cluster size due to the specific interactions between the anionic species and a few glyphosate molecules. Hence, these systems are useful for discussing $[Cu(opba)]^{2-}$-GLY interactions but should be considered as a model for solvation. This is evident when comparing the experimental absorption spectra shown in the supplementary material, Figure S3. Indeed, they look identical, since the amount of GLY is so high that the spectra merge together and resemble that of plain GLY shown in Figure S1c. Improved models were provided by "symmetric solvated $[Cu(opba)]^{2-}$" such as $[Cu(opba)]^{2-}(GLY)_4$ and $[Cu(opba)]^{2-}(GLY)_4$+SCRF, which are discussed in detail below.

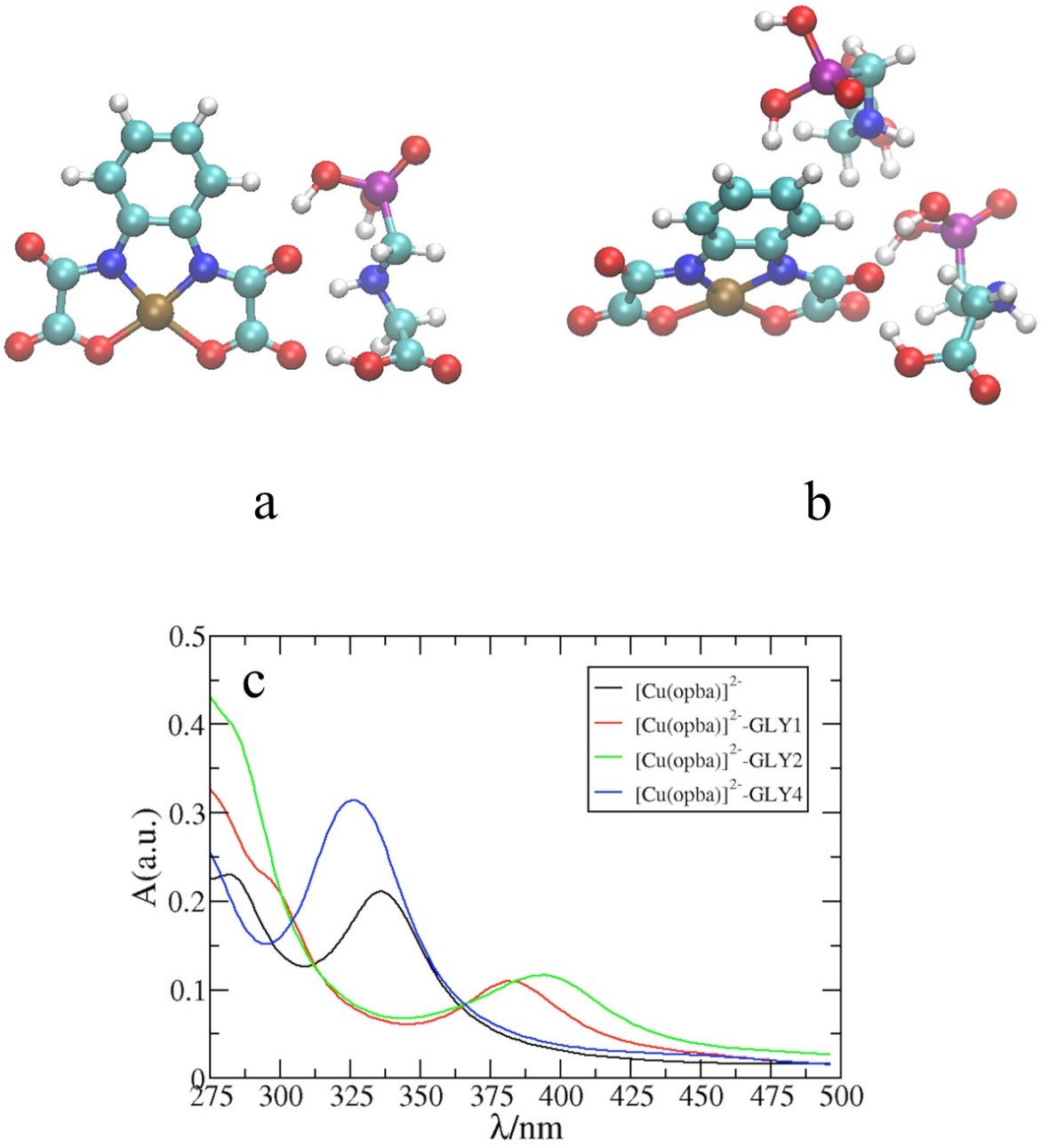

Figure 7. (**a**,**b**) B3LYP/SDD optimized structures of $[Cu(opba)]^{2-}(GLY)_N$ (N = 1, 2); Atom colors: copper (brown); carbon (cyan); nitrogen (blue); oxygen (red); hydrogen (white); phosphorous (magenta). O . . . H(GLY) hydrogen bond distances (in Å) are: 1.62 (N = 1); 1.63; 1.67 (N = 2). (**c**) Absorption spectra of $[Cu(opba)]^{2-}(GLY)_N$ (N = 1–4).

Figure 8 depicts the structure of $[Cu(opba)]^{2-}(GLY)_4$, which was used to calculate the absorption spectra using the MS and MS+SCRF models. The selection of this structure was based on the almost symmetrical arrangement of the complex, which will be placed in a dielectric medium in the MS+SCRF method. The figure also shows the formation of hydrogen bonds, where glyphosate primarily acts as a proton donor. The comparison between the results obtained from MS and MS+SCRF models for the absorption spectrum supports the notion that long-range polarization effects cause an ~16 nm red-shift of the main absorption maximum of the ionic species.

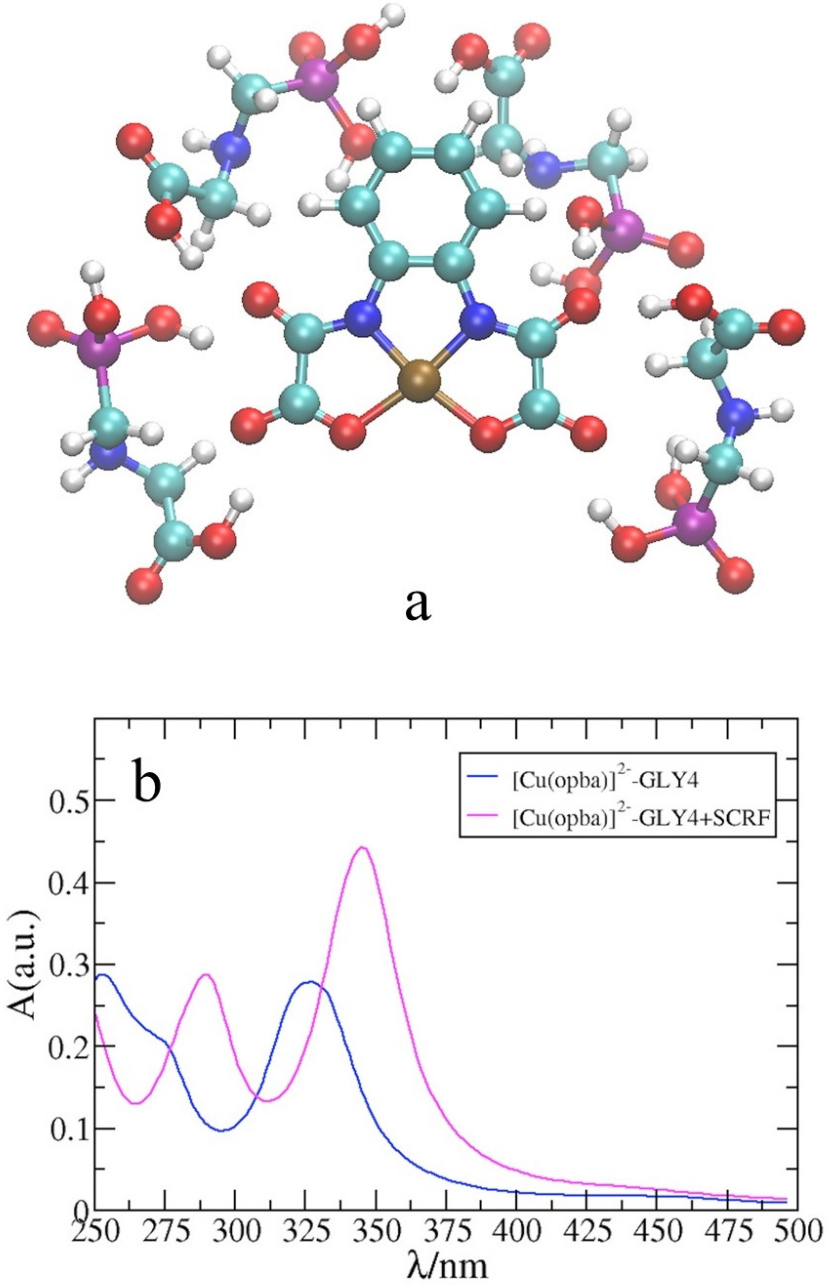

Figure 8. (**a**) B3LYP/SDD optimized structure of $[Cu(opba)]^{2-}(GLY)_4$. Atom colors: copper (brown); carbon (cyan); nitrogen (blue); oxygen (red); hydrogen (white); phosphorous (magenta). Some O . . . H(GLY) hydrogen bond distances (in Å) are: 1.66; 1.76; 1.78. (**b**) Absorption spectra from MS (blue) and MS+SCRF (magenta).

Emission Spectra

The emission spectrum of $[Cu(opba)]^{2-}$ in ACN and GLY is presented in Figure 9. In ACN, the emission spectra (Figure 9a) were calculated by combining the emission spectra corresponding to excitations at λ = 344.0 nm, which is the lowest excited state with the same multiplicity (S = 2) of $[Cu(opba)]^{2-}$ and λ = 266.5 nm, which is a higher energy state. Comparison between the theoretical and experimental results for the emission spectrum (see Table 2) shows a good agreement, mainly for the positions of second maximum that are at 420 nm (theoretical) and 400 nm (present experimental). However, the theoretical prediction for the position of the first maximum (349.2 nm) is ~18 nm lower than the experimental value. We noticed that by including the two excited states referred to

above, a better agreement with experiment was observed, suggesting some deviation from Kasha's rule [46].

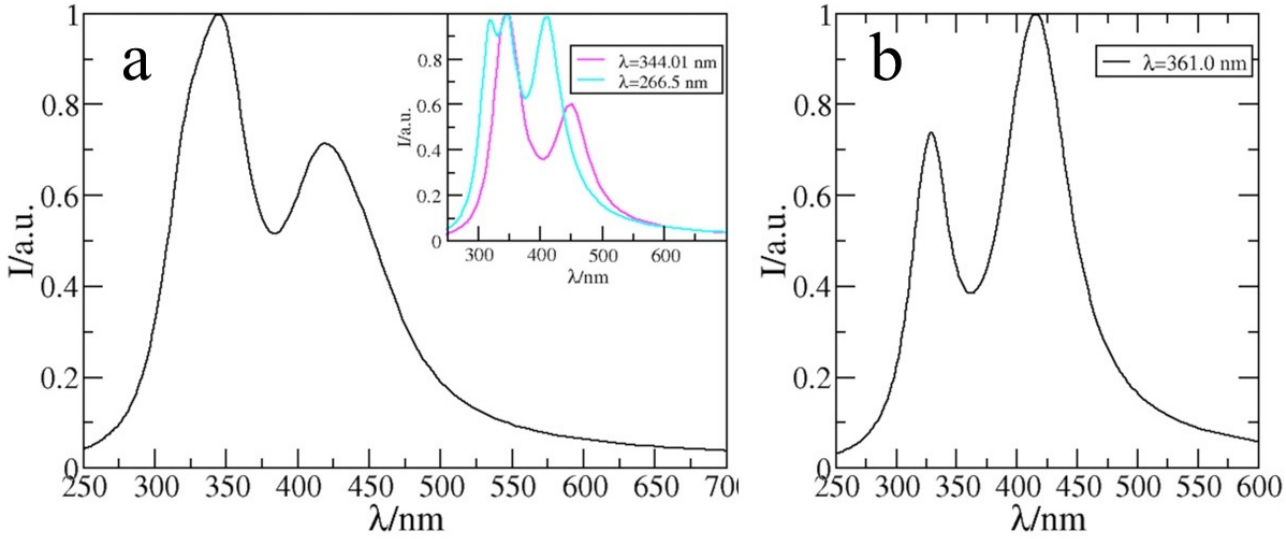

Figure 9. TDDFT emission spectrum of solvated $[Cu(opba)]^{2-}$ in (**a**) ACN, ε = 35.69. Inset shows emission spectra for excitations at a given λ; (**b**) in formamide, ε = 108.9.

Table 2. $[Cu(opba)]^{2-}$ absorption and emission energies (in nm).

Complex	SCRF	MS	MS+SCRF	Exp./Others
$[Cu(opba)]^{2-}$ + ACN	ε = 35.69	$[Cu(opba)]^{2-}$-ACN6	$[Cu(opba)]^{2-}$-ACN6 + ε	
Absorption	266.5(0.11); 344.0(0.20)	335.9(0.13)	288.0(0.01); 340.9(0.19)	330.0
Emission	349.2; 420.3			368.0; 400.0
$[Cu(opba)]^{2-}$ + GLY	ε = 108.9	$[Cu(opba)]^{2-}$-GLY4	$[Cu(opba)]^{2-}$-GLY4 + ε	
Absorption	273.6(0.07); 361.0(0.27)	331.9(0.04)	291.9; 347.6	
Emission	329.6; 415.4			375.0; 410

Figure 9b displays the emission spectra of $[Cu(opba)]^{2-}$ in GLY, characterized by two maxima at 329.6 nm and 415.4 nm upon excitation at 361 nm. Comparison with the emission of $[Cu(opba)]^{2-}$ in ACN shows an increase in the intensity of the second peak relative to the first. This trend appears to agree with the present experimental results for the emission spectra of $[Cu(opba)]^{2-}$ in GLY, where the intensity of the second peak increases with increasing glyphosate concentration. This effect is linked to higher values of the dielectric constant [43] or stronger polarization effects. Moreover, the experimental emission spectra of $[Cu(opba)]^{2-}(GLY)_N$ (N = 1, 2, and 4) species shown in Figure S4 exhibit similar features, especially when recorded under 350 nm excitation.

Theoretical results for the absorption and emission spectra of $[Cu(opba)]^{2-}$ in ACN and GLY obtained using different theoretical methods are collected in Table 2. Generally, experimental and theoretical results were in good agreement, with differences below 0.2 eV. For the emission spectra, specifically for the case of $[Cu(opba)]^{2-}$ in GLY, comparison between the first peak position between SCRF prediction and experiment led to a difference of −0.46 eV, while a very good agreement was observed for the second peak. We noticed that in this case, the dielectric constant was estimated as that of formamide, and the exact values for the experimental conditions were not known. Relative intensities predicted by SCRF showed some differences when compared to experiment. However, it should be noted that the intensities were related to oscillator strengths that, in general, are very dependent on the DFT/SCRF combination.

4. Conclusions

A new optical method for detecting glyphosate was investigated using a copper bis(oxamate) complex, namely $[^nBu_4N]_2[Cu(opba)]$, as the fluorescent probe. Unlike molecular probes containing copper, this probe interacts with glyphosate molecules through hydrogen bonding, causing an increase in the local dielectric constant and enhancing light emission. This method offers a simple and effective way to detect glyphosate at environmental levels, with a limit of detection below the maximum residual limit for glyphosate in drinking water established by international regulations.

Supplementary Materials: The following supporting information can be downloaded at: https://www.mdpi.com/article/10.3390/chemosensors11030194/s1, Figure S1 (Spectroscopic characteristics of [nBu4N]2[Cu(opba)]), Figure S2 (Emission spectra of $[Cu(opba)]^{2-}$ as a function of the excitation wavelength), Figure S3 (UV-Vis absorption spectra of $[Cu(opba)]^{2-}$-(GLY)-1,2,4 complexes), Figure S4 (Emission spectra of $[Cu(opba)]^{2-}$-(GLY)-1,2,4 complexes at 270 nm and 350 nm excitations), Table S1 (Assignment of FTIR and Raman bands for [nBu4N]2[Cu(opba)]). [28–31]

Author Contributions: Conceptualization, G.M., B.J.C.C. and L.G.P.; methodology, G.M., K.V.O. and S.W.; software, B.J.C.C.; validation, G.M., B.J.C.C. and L.G.P.; formal analysis, G.M., B.J.C.C. and L.G.P.; investigation, G.M., K.V.O., S.W. and B.J.C.C.; resources, O.K., B.J.C.C. and L.G.P.; data curation, G.M., K.V.O., S.W. and B.J.C.C.; writing—original draft preparation, G.M., B.J.C.C. and L.G.P.; writing—review and editing, S.W., A.A.-H., O.K., T.R., B.J.C.C. and L.G.P.; visualization, L.G.P.; supervision, L.G.P.; project administration, O.K. and L.G.P.; funding acquisition, O.K. and L.G.P. All authors have read and agreed to the published version of the manuscript.

Funding: This research was funded by Conselho Nacional de Desenvolvimento Científico e Tecnológico (CNPq), Coordenação de Aperfeiçoamento de Pessoal de Nível Superior (Capes), finance code 001, Fundação de Apoio à Pesquisa do Distrito Federal (FAPDF), grant number 00193. 00001824/2022-64, and Deutsche Forschungsgemeinschaft (DFG), grant number 1663/13-1.

Institutional Review Board Statement: Not applicable.

Informed Consent Statement: Not applicable.

Data Availability Statement: Data are available from the authors upon reasonable request.

Acknowledgments: The authors are thankful to the Brazilian funding agencies CNPq, CAPES and FAPDF and German agency DFG.

Conflicts of Interest: The authors declare no conflict of interest.

References

1. Gillezeau, C.; van Gerwen, M.; Shaffer, R.M.; Rana, I.; Zhang, L.; Sheppard, L.; Taioli, E. The Evidence of Human Exposure of Glyphosate: A Review. *J. Environ. Health* **2019**, *18*, 2–14. [CrossRef] [PubMed]
2. Steinruck, H.C.; Amrhein, N. The Herbicide Glyphosate is a Potent Inhibitor of 5-Enolpyruvyl-Shikimic Acid-3-Phoshate Synthase. *Biochem. Biophys. Res. Comm.* **1980**, *94*, 1207–1212. [CrossRef] [PubMed]
3. Dill, G.M.; Sammons, R.D.; Feng, P.C.C.; Kohn, F.; Kretzmer, K.; Mehrsheikh, A.; Bleeke, M.; Honegger, J.L.; Farmer, D.; Wright, D.; et al. Glyphosate: Discovery, Development, Applications and Properties. In *Glyphosate Resistance in Crops and Weeds: History, Development and Management*, 1st ed.; Nandula, V.K., Ed.; Wiley: Hoboken, NJ, USA, 2010; pp. 1–66.
4. Ghisi, N.C.; Zuanazzi, N.R.; Fabrin, T.M.C.; Oliveira, E.C. Glyphosate and its Toxicology: A Scientometric Review. *Sci. Total Environ.* **2020**, *733*, 139359. [CrossRef] [PubMed]
5. Valle, A.L.; Mello, F.C.C.; Alves-Balvedi, R.P.; Rodrigues, L.P.; Goulart, L.R. Glyphosate Detection: Methods, Needs and Challenges. *Environ. Chem. Lett.* **2019**, *17*, 291–317. [CrossRef]
6. Fang, F.; Wei, R.; Liu, X. Novel Pre-Column Derivatization Reagent for Glyphosate by High-Performance Liquid Chromatography and Ultraviolet Detection. *Int. J. Environ. Anal. Chem.* **2014**, *94*, 661–667. [CrossRef]
7. Suna, L.; Kong, D.; Gu, W.; Guo, X.; Tao, W.; Shan, Z.; Wang, Y.; Wang, N. Determination of Glyphosate in Soil/Sludge by High Performance Liquid Chromatography. *J. Chromatogr. A* **2017**, *1502*, 8–13. [CrossRef] [PubMed]
8. Tiago, J.P.F.; Sucupira, L.C.; Barros, R.E.; de Pinho, G.P.; Silvério, F.O. Simultaneous and Direct Determination of Glyphosate and AMPA in Water Samples from the Hydroponic Cultivation of Eucalyptus Seedlings Using HPLC-ICP-MS/MS. *J. Environ. Sci. Health B* **2020**, *55*, 558–565. [CrossRef]
9. Crocoli, L.C.; Ortiz, R.S.; Moura, S. Development and Validation of q-NMR Method for Analyses of Legal and Illegal Formulations of Glyphosate. *Anal. Methods* **2019**, *11*, 4052–4059. [CrossRef]

10. Zhao, J.; Pacenka, S.; Wu, J.; Richards, B.K.; Steenhuis, T.; Simpson, K.; Hay, A.G. Detection of Glyphosate Residues in Companion Animal Feeds. *Environ. Poll.* **2018**, *243*, 1113–1118. [CrossRef]
11. Clegg, B.S.; Stephenson, G.R.; Hall, J.C. Development of an Enzyme-Linked Immunosorbent Assay for the Detection of Glyphosate. *J. Agric. Food Chem.* **1999**, *47*, 5031–5037. [CrossRef]
12. Tu, Q.; Yang, T.; Qu, Y.; Gao, S.; Zhang, Z.; Zhang, Q.; Wang, Y.; Wang, J.; He, L. In Situ Colorimetric Detection of Glyphosate on Plant Tissues Using Cysteamine-Modified Gold Nanoparticles. *Analyst* **2019**, *144*, 2017–2025. [CrossRef] [PubMed]
13. Moraes, F.C.; Mascaro, L.H.; Machado, S.A.S.; Brett, C.M.A. Direct Electrochemical Determination of Glyphosate at Copper Phthalocyanine/Multiwalled Carbon Nanotube Film Electrodes. *Electroanalysis* **2010**, *22*, 1586–1591. [CrossRef]
14. Congur, G. An Up-to-Date Review About (Bio)Sensor Systems Developed for Detection of Glyphosate. *Int. J. Environ. Anal. Chem.* **2021**, 1–13. [CrossRef]
15. Prerna, Y.; Zelder, F. Detection of Glyphosate with a Copper(II)-Pyrocatechol Violet Based GlyPKit. *Anal. Methods* **2021**, *13*, 4354–4360.
16. Wang, L.; Bi, Y.; Hou, J.; Li, H.; Xu, Y.; Wang, B.; Ding, H.; Ding, L. Facile, Green and Clean One-Step Synthesis of Carbon Dots from Wool: Application as a Sensor for Glyphosate Detection Based on the Inner Filter Effect. *Talanta* **2016**, *160*, 268–275. [CrossRef] [PubMed]
17. Yuan, Y.; Jiang, J.; Liu, S.; Yang, J.; Zhang, H.; Yan, J.; Hu, X. Fluorescent Carbon Dots for Glyphosate Determination Based on Fluorescence Resonance Energy Transfer and Logic Gate Operation. *Sens. Actuators B Chem.* **2017**, *242*, 545–553. [CrossRef]
18. Jiménez-López, J.; Llorent-Martínez, E.J.; Ortega-Barrales, P.; Ruiz-Medina, A. Graphene Quantum Dots-Silver Nanoparticles as a Novel Sensitive and Selective Luminescence Probe for the Detection of Glyphosate in Food Samples. *Talanta* **2020**, *207*, 120344. [CrossRef]
19. Fang, H.; Zhang, X.; Gao, D.; Xiao, Y.; Ma, L.; Yang, H.; Zhou, Y. Fluorescence Determination of Glyphosate Based on a DNA-Templated Copper Nanoparticle Biosensor. *Microchim. Acta.* **2022**, *189*, 158. [CrossRef]
20. Wang, D.; Lin, B.; Cao, Y.; Guo, M.; Yu, Y. A Highly Selective and Sensitive Fluorescence Detection Method of Glyphosate Based on an Immune Reaction Strategy of Carbon Dot Labeled Antibody and Antigen Magnetic Beads. *J. Agric. Food Chem.* **2016**, *64*, 6042–6050. [CrossRef]
21. Gui, M.; Jiang, J.; Wang, X.; Yan, Y.; Li, S.; Xiao, X.; Liu, T.; Feng, Y. Copper Ion-Mediated Glyphosate Detection with N-Heterocycle Based Polyacetylene as a Sensing Platform. *Sens. Actuators B Chem.* **2017**, *243*, 696–703. [CrossRef]
22. Sun, F.; Ye, X.L.; Wang, Y.B.; Yue, M.L.; Li, P.; Yang, L.; Liu, Y.L.; Fu, Y. NPA-Cu^{2+} Complex as a Fluorescent Sensing Platform for the Selective and Sensitive Detection of Glyphosate. *Int. J. Mol. Sci.* **2021**, *22*, 9816. [CrossRef] [PubMed]
23. Wang, X.; Sakinati, M.; Yang, Y.; Ma, Y.; Yang, M.; Luo, H.; Houa, C.; Huo, D. The construction of a CND/Cu^{2+} fluorescence sensing system for the ultrasensitive detection of glyphosate. *Anal. Methods* **2020**, *12*, 520–527. [CrossRef]
24. Coutinho, C.F.B.; Mazo, L.H. Metallic Complexes with Glyphosate: A Review. *Química Nova* **2005**, *28*, 1038–1045. [CrossRef]
25. Hance, R.J. Herbicide Usage and Soil Properties. *Plant Soil* **1976**, *45*, 291–293. [CrossRef]
26. Arroyave, J.M.; Waiman, C.C.; Zanini, G.P.; Avena, M.J. Effect of Humic Acid on the Adsorption/Desorption Behavior of Glyphosate on Goethite. Isotherms and Kinetics. *Chemosphere* **2016**, *145*, 34–41. [CrossRef]
27. McNaughton, D.A.; Fares, M.; Picci, G.; Gale, P.A.; Caltagiron, C. Advances in Fluorescent and Colorimetric Sensors for Anionic Species. *Coord. Chem. Rev.* **2021**, *427*, 213573. [CrossRef]
28. Abdulmalic, M.A.; Aliabadi, A.; Petr, A.; Kataev, V.; Rüffer, T. The Formation of Overlooked Compounds in The Reaction of Methyl Amine with the Diethyl Ester of *o*-Phenylenebis(oxamic acid) in MeOH. *Dalton Trans.* **2013**, *42*, 1798–1809. [CrossRef]
29. Weheabby, S.; Al-Shewiki, R.K.; Hildebrandt, A.; Abdulmalic, M.A.; Lang, H.; Rüffer, T. Electrochemical Studies of the $M^{I/II}$ and $M^{II/III}$ (M = Ni, Cu) Couples in Mono- to Tetranuclear Complexes with Oxamato/Oxamidato Ligands. *Electrochim. Acta* **2019**, *318*, 181–193. [CrossRef]
30. Cervera, B.; Sanz, J.L.; Ibáñez, M.J.; Vila, G.; Loret, F.L.; Julve, M.; Ruiz, R.; Ottenwaelder, X.; Aukauloo, A.; Poussereau, S.; et al. Stabilization of Copper(III) Complexes by Substituted Oxamate Ligands. *J. Chem. Soc. Dalton Trans.* **1998**, 781–790. [CrossRef]
31. do Nascimento, G.M.; do Pim, W.; Reis, D.O.; Simões, T.R.G.; Pradie, N.A.; Stumpf, H.O. Characterization of Compounds Derived from Copper-Oxamate and Imidazolium by X-Ray Absorption and Vibrational Spectroscopies. *Spectrochim. Acta Part A Mol. Biomol. Spectrosc.* **2015**, *142*, 303–310. [CrossRef]
32. Lupi, L.; Miglioranza, K.S.B.; Aparicio, V.C.; Marino, D.; Bedmar, F.; Wunderlin, D.A. Occurrence of Glyphosate and AMPA in an Agricultural Watershed from the Southeastern Region of Argentina. *Sci. Total Environ.* **2015**, *536*, 687–694. [CrossRef] [PubMed]
33. Dourado, C.S.; Lins, E.S.; Dias, A.C.B. Development of a Sequential Injection System with Online Photo-Cleavage Coupled to SPE for Spectrophotometric Determination of N-Nitrosoglyphosate. *Microchem. J.* **2019**, *147*, 1061–1067. [CrossRef]
34. Becke, A.D. Density-Functional Exchange-Energy Approximation with Correct Asymptotic Behavior. *Phys. Rev. A* **1988**, *38*, 3098–3100. [CrossRef] [PubMed]
35. Lee, C.; Yang, W.; Parr, R.G. Development of the Colle-Salvetti Correlation-Energy Formula into a Functional of the Electron Density. *Phy. Rev. B* **1988**, *37*, 785–789. [CrossRef] [PubMed]
36. Dunning, T.; Hay, P. *Modern Theoretical Chemistry*; Schaefer, H.F., Ed.; Plenum Press: New York, NY, USA, 1976; ISBN 978-1-4757-0889-9.
37. Marenich, A.V.; Olson, R.M.; Kelly, C.P.; Cramer, C.J.; Truhlar, D.G. Self-Consistent Reaction Field Model for Aqueous and Nonaqueous Solutions Based on Accurate Polarized Partial Charges. *J. Chem. Theory Comput.* **2007**, *3*, 2011–2033. [CrossRef] [PubMed]

38. Lipparini, F.; Mennucci, B. Perspective: Polarizable Continuum Models for Quantum-Mechanical Descriptions. *J. Chem. Phys.* **2016**, *144*, 160901. [CrossRef]
39. Marenich, A.V.; Cramer, C.J.; Truhlar, D.G. Universal Solvation Model Based on Solute Electron Density and on a Continuum Model of the Solvent Defined by the Bulk Dielectric Constant and Atomic Surface Tensions. *J. Phys. Chem. B* **2009**, *113*, 6378–6396. [CrossRef]
40. Stewart, J.J.P. Optimization of Parameters for Semiempirical Methods V: Modification of NDDO Approximations and Application to 70 Elements. *J. Mol. Model.* **2007**, *13*, 1173–1213. [CrossRef]
41. Maitra, N.T.; Wasserman, A.; Burke, K. What is Time-Dependent Density Functional Theory? Successes and Challenges. In *Electron Correlations and Materials Properties 2*; Springer: New York, NY, USA, 2003; pp. 285–298, ISBN 978-0-306-47446-0.
42. Wang, J.; Durbeej, B. How Accurate Are TD-DFT Excited-State Geometries Compared to DFT Ground-State Geometries? *J. Comput. Chem.* **2020**, *41*, 1718–1729. [CrossRef]
43. Zamora, J.L.; Vargas, D.R.; Hernández-Gómez, Y.K.; Álvarez-Botero, G.A. Improvement the Permittivity Determination in Glyphosate-Water Mixture Using CSRR as Sensor. In Proceedings of the 2018 IEEE International Instrumentation and Measurement Technology Conference (I2MTC), Houston, TX, USA, 14–17 May 2018; pp. 1–5.
44. Costa, I.A.; Gross, M.A.; Alves, E.D.O.; Fonseca, F.J.; Paterno, L.G. An Impedimetric E-Tongue Based on CeO_2-Graphene Oxide Chemical Sensors for Detection of Glyphosate and Its Potential Interferents. *J. Electroanal. Chem.* **2022**, *922*, 116719. [CrossRef]
45. Frisch, M.J.; Trucks, G.W.; Schlegel, H.B.; Scuseria, G.E.; Robb, M.A.; Cheeseman, J.R.; Scalmani, G.; Barone, V.; Petersson, G.A.; Nakatsuji, H.; et al. *Gaussian 16*; revision C.01; Gaussian, Inc.: Wallingford, CT, USA, 2016.
46. del Valle, J.C.; Catalan, J. Kasha's Rule: A Reappraisal. *Phys. Chem. Chem. Phys.* **2019**, *21*, 10061–10069. [CrossRef] [PubMed]